

Rational Design of Dehydrogenase/Reductases Based on Comparative Structural Analysis of Prereaction-State and Free-State Simulations for Efficient Asymmetric Reduction of Bulky Aryl Ketones

Bing-Mei Su,^{†,‡,§} Ze-Hui Shao,[§] Ai-Peng Li,^{||} Muhammad Naeem,[‡] Juan Lin,^{*,†,‡} Li-Dan Ye,^{*,‡,§} and Hong-Wei Yu^{*,‡,§}

[†]College of Chemical Engineering, Fuzhou University, Fuzhou 350116, China

[‡]Institute of Bioengineering, College of Chemical and Biological Engineering, Zhejiang University, Hangzhou 310027, China

[§]College of Pharmaceutical Science, Zhejiang University of Technology, Hangzhou 310027, China

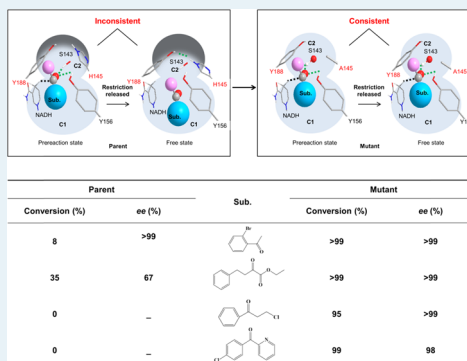
^{||}School of Life Sciences, Northwestern Polytechnical University, Xi'an 710072, China

[¶]College of Biological Science and Engineering, Fuzhou University, Fuzhou 350116, China

Supporting Information

ABSTRACT: Inspired by the conformational change of the enzyme–substrate complex in molecular dynamics (MD) simulation with distance restriction, we propose a strategy for identifying the engineering targets based on the comparative analysis of enzyme-/substrate-binding modes in MD simulations with and without distance restriction (prereaction-state simulation and free-state simulation). Taking the short-chain dehydrogenase/reductase (SDR) mutant EbSDR8-G94A/S153L (Mu0) with poor activity toward bulky aryl ketones as an example, H145 and Y188 were identified as the engineering targets due to the distinct conformation difference in the two simulation modes. To break the “beam” structure formed by these residues at the entry of cavity C2 in free-state simulation, the substrate-binding pocket was reconstructed, and meanwhile the relative size of cavities C1 and C2 was modulated to improve the enantioselectivity. In this way, mutants for efficient asymmetric reduction of o-halogenated acetophenones, propiophenones, aromatic ketoesters, and diaryl ketones were designed, delivering chiral alcohols with >99% conversion and >98% ee. The effectiveness of this design strategy was also validated by the successful redesign of PpYSDR, generating a variant for efficient reduction of (4-chlorophenyl) 2-pyridyl ketone into the *S*-product with >99% conversion and 96% ee. MD simulations suggested a suitable binding pocket with proper energy contribution as the ubiquitous mechanism for the improvement of activity and enantioselectivity toward substrates with varied structures. The success in this study provides hints for the rational design of alcohol dehydrogenases/reductases with both a broad substrate spectrum and high enantioselectivity.

KEYWORDS: alcohol dehydrogenase/reductase, protein engineering, enantioselectivity, prereaction-state simulation, free-state simulation, energy contribution



INTRODUCTION

Chiral alcohols are important building blocks of complex compounds, with wide applications in pharmacy,^{1,2} agricultural chemistry,³ and fragrance⁴ and fine chemical industries.⁵ Asymmetric bioreduction of prochiral ketones employing dehydrogenases/reductases is an important method for the preparation of chiral alcohols.⁶ However, for the unnatural substrates of industrial interest, the native enzymes often suffer from limited activity or insufficient enantioselectivity.

Protein engineering has demonstrated its power in improving the catalytic performance of enzymes.^{7–9} For the mutants generated by protein engineering, computational molecular dynamics simulation has been widely employed to

interpret the mechanism responsible for the change in enzyme features such as activity, stability, and enantioselectivity.^{7,10} The emergence of constrained MD simulation made the analysis of the prereaction state possible, and since then, the difference in formation probability and stability of the prereaction state was used to explain the activity difference in various reaction systems.^{11–13} Constrained MD simulation applies an external force onto a physical system, which drives a change in coordinates.^{14,15} Hence, we put forward a

Received: November 5, 2019

Revised: December 3, 2019

Published: December 4, 2019



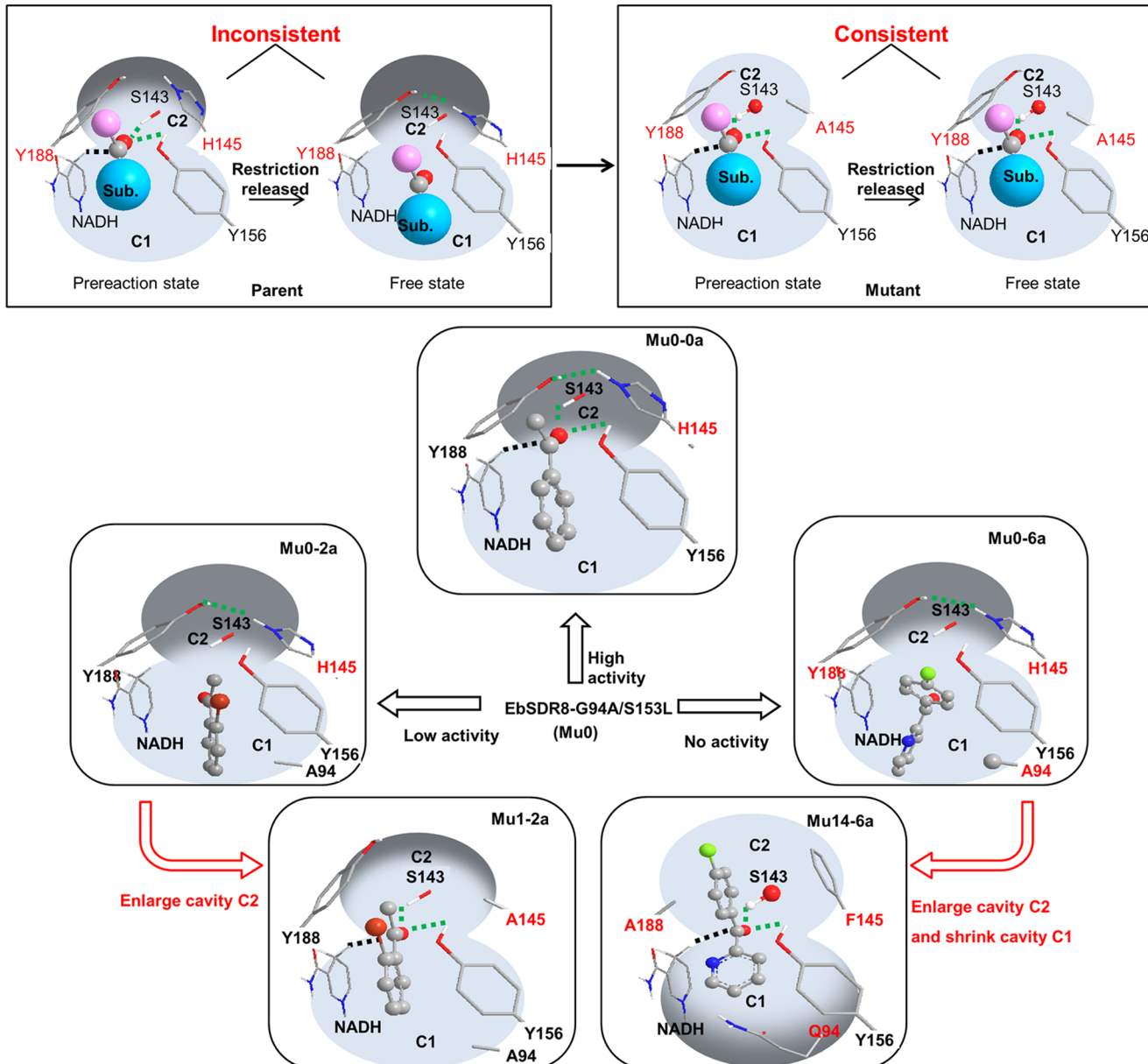


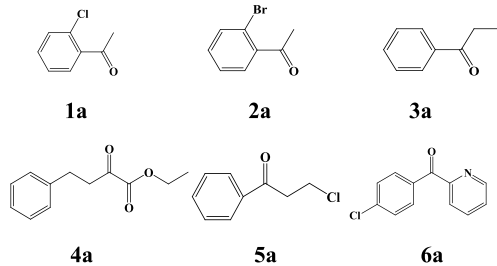
Figure 1. Redesign of EbSDR8-G94A/S153L (Mu0). Key residues are shown as sticks, and the substrates are shown as balls and sticks. The green dashes represent the hydrogen bonds. The black dashes represent the transfer of hydride.

hypothesis: the binding mode of the substrate/enzyme complex in prereaction-state simulation (with distance restriction, defined as T-state simulation) would be distinctly different from that in free-state simulation (without distance restriction, defined as F-state simulation) if the binding pocket is not suitable for accommodating the target substrate. Based on this hypothesis, a strategy is proposed to identify the engineering targets for enzyme redesign toward unnatural substrates by searching for the key residues with obviously different conformations in T-state simulation and F-state simulation.

In our previous study, a short-chain dehydrogenase/reductase (SDR) from *Empedobacter brevis* ZJUY-1401 (EbSDR8, GenBank: ALZ42979.1) was discovered to be an excellent dehydrogenase/reductase for R-selective reduction of prochiral aryl ketones to the corresponding alcohols,^{16,17} and its catalytic efficiency was further improved by G94A/S153L double mutations.⁸ However, Mu0 (EbSDR8-G94A/S153L)

showed poor activity toward bulky aryl ketones such as halogenated acetophenones, propiophenones, aromatic ketoesters, and diaryl ketones that are highly demanded in pharmaceuticals, agricultural chemistry, fragrance, and fine chemical industries.^{10,11,18,19} In this study, the structural basis preventing the catalysis of 2'-bromoacetophenone (**2a**) by Mu0 is revealed via enzyme–substrate docking and molecular dynamics (MD) simulations for T-state and F-state so as to identify the engineering targets.

To obtain mutants with both a broadened substrate spectrum and high enantioselectivity, the relative size of the two cavities in the “gourd”-like substrate-binding pocket should be taken into consideration during reconstruction of the substrate-binding pocket to accommodate the target bulky substrate. According to Prelog’s rule,²⁰ a binding pocket composed of a smaller cavity C1 and a larger cavity C2 leads to S-selectivity,²¹ whereas a larger C1 and a smaller C2 typically constitute the binding pocket of an R-selective enzyme²²

Table 1. Mutagenesis at Positions 145 and 188 of EbSDR8-G94A/S153L^a

enzyme	description	sub. ^b	conversion (%)	ee (%)	sub.	conversion (%)	ee (%)
E	EbSDR8	1a	>99	>99 (R)	2a	ND ^c	NA ^d
Mu0	E-G94A/S153L		>99	>99 (R)		8.0	>99 (R)
Mu1	Mu0-H145A		>99	>99 (R)		>99	>99 (R)
Mu2	Mu0-H145C		>99	>99 (R)		>99	>99 (R)
Mu3	Mu0-H145G		>99	>99 (R)		93	>99 (R)
Mu4	Mu0-Y188A		>99	89 (R)		25	22 (R)
Mu5	Mu0-Y188C		11	>99 (R)		12	95 (R)
Mu6	Mu0-Y188G		>99	87 (R)		14	18 (R)
E	EbSDR8	3a	4.0	>99 (R)	4a	ND	NA
Mu0	E-G94A/S153L		38	>99 (R)		35	67 (S)
Mu1	Mu0-H145A		92	>99 (R)		>99	51 (S)
Mu2	Mu0-H145C		93	>99 (R)		>99	82 (S)
Mu3	Mu0-H145G		74	>99 (R)		>99	40 (R)
Mu4	Mu0-Y188A		95	>99 (R)		>99	>99 (S)
Mu5	Mu0-Y188C		63	>99 (R)		>99	94 (S)
Mu6	Mu0-Y188G		84	>99 (R)		>99	>99 (S)
E	EbSDR8	5a	ND	NA	6a	ND	NA
Mu0	E-G94A/S153L		ND	NA		ND	NA
Mu1	Mu0-H145A		90	94 (R)		ND	NA
Mu2	Mu0-H145C		ND	NA		ND	NA
Mu3	Mu0-H145G		59	>99 (R)		ND	NA
Mu4	Mu0-Y188A		95	>99 (R)		ND	NA
Mu5	Mu0-Y188C		ND	NA		ND	NA
Mu6	Mu0-Y188G		92	96 (R)		ND	NA

^aExperiments were performed in triplicate, and mean values are presented. ^bSub. = substrate. ^cND = not detected. ^dNA = not available.

(Figure S1A,B). The same phenomenon is found in esterases and lipases, named as the Kazlauskas rule, which is widely applied to predict, explain, and improve the enantioselectivity of these enzymes.^{23–25} Therefore, Mu0 was redesigned for efficient asymmetric reduction of various prochiral ketones under the guidance of T-/F-state comparative analysis and Prelog's rule (Figure 1). The design principle and strategy are further validated by structural modification of PpYSDR for efficient S-selective reduction of (4-chlorophenyl) 2-pyridyl ketone (**6a**).

RESULTS AND DISCUSSION

EbSDR8-G94A/S153L Was Unable To Reduce Prochiral Aryl Ketones with Bulky Side Chains. Mu0 (EbSDR8-G94A/S153L) was designed for excellent anti-Prelog reduction of prochiral aryl ketones with an aromatic ring and a methyl or halogenated methyl at the carbonyl carbon.⁸ However, its activity toward prochiral aryl ketones with larger substituents at the carbonyl carbon was rather low. In whole-cell reduction of 50 mM prochiral aryl ketones, Mu0 showed poor efficiency in the reduction of 2'-bromoacetophenone (**2a**), propiophenone (**3a**), and 2-oxo-4-phenylbutyrate (**4a**) with less than 40% conversion and failed to reduce 3-chloropropiophenone (**5a**) and (4-chlorophenyl) 2-pyridyl ketone (**6a**) (Table 1).

Determination of catalytic kinetics showed that the turnover number (k_{cat}) values of EbSDR8 (E) and its mutant Mu0 for all testing substrates were less than 0.1/s or unavailable due to severe substrate inhibition (Table 2). The substituent at *o*-position of the aromatic ring had a big influence on the activity, as demonstrated by the obviously lower activity of **2a** than **1a**. The k_{cat} decreased by a large margin as the substituent at *o*-position enlarged from chlorine to bromine. Similar results were observed for **3a** and **5a**.

The results of whole-cell reduction and catalytic kinetics suggested that the substrate-binding pocket of Mu0 may not be suitable for accommodating prochiral aryl ketones with bulky side chains. Widening the substrate spectrum of Mu0 by restructuring the substrate-binding pocket with rational design may help pave its way to industrial applications.

Modeling and Simulation Suggested the “Beam” Formed by H145 and Y188 as a Possible Hindrance. To explore the reason for Mu0's limited substrate spectrum, the structural model of the Mu0 holoenzyme was built by homologous modeling²⁶ and MD simulation.²⁷ The predicted model of Mu0 was assessed to be reasonable with a VERIFY value of 96% and an ERRAT value of 93, and >99% of the residues were located in the allowed region as suggested by the Ramachandran plot. As shown in Figure S1C, the substrate-binding pocket of Mu0 has a “gourd” shape, which is

Table 2. Apparent Kinetic Parameters of EbSDR8 and Its Variants^a

sub. ^b	enzyme	description	K_m (mM)	k_{cat} (1/s)	k_{cat}/K_m (1/mM/s)
1a	E	EbSDR8	2.2×10^{-1}	2.0×10^{-2}	1.1×10^{-1}
	Mu0	E-G94A/S153L	1.5×10^{-1}	1.0×10^{-1}	7.0×10^{-1}
	Mu1	Mu0-H145A	2.1×10^{-1}	9.7×10^{-1}	4.6
	Mu2	Mu0-H145C	2.3×10^{-1}	2.8×10^{-1}	1.2
	Mu3	Mu0-H145G	1.3	1.2	9.3×10^{-1}
2a	E	EbSDR8	2.0×10^{-2}	1.0×10^{-2}	5.4×10^{-1}
	Mu0	E-G94A/S153L	7.0×10^{-1}	3.0×10^{-2}	5.0×10^{-2}
	Mu1	Mu0-H145A	9.0×10^{-2}	1.1	1.2×10
	Mu2	Mu0-H145C	4.0×10^{-2}	1.5×10^{-1}	3.7
	Mu3	Mu0-H145G	2.0	6.9×10^{-1}	3.5×10^{-1}
3a	E	EbSDR8	1.0×10^{-1}	1.0×10^{-2}	1.4×10^{-1}
	Mu0	E-G94A/S153L	9.0×10^{-2}	7.0×10^{-2}	8.1×10^{-1}
	Mu1	Mu0-H145A	3.0×10^{-1}	7.5×10^{-1}	2.5
	Mu2	Mu0-H145C	6.0×10^{-2}	7.0×10^{-2}	1.2
	Mu4	Mu0-Y188A	5.5×10^{-1}	5.1×10^{-1}	9.1×10^{-1}
4a	E	EbSDR8	NA ^c	NA	NA
	Mu0	E-G94A/S153L	1.0×10^{-2}	3.0×10^{-2}	5.5
	Mu4	Mu0-Y188A	1.8×10^{-1}	2.5×10	1.4×10^2
	Mu6	Mu0-Y188G	4.0×10^{-1}	5.2×10	1.3×10^2
5a	E	EbSDR8	3.0×10^{-2}	2.0×10^{-2}	6.3×10^{-1}
	Mu0	E-G94A/S153L	9.0×10^{-2}	6.0×10^{-2}	6.6×10^{-1}
	Mu4	Mu0-Y188A	5.4×10^{-1}	1.23	2.29
6a	E	EbSDR8	3.0×10^{-2}	1.0×10^{-2}	4.2×10^{-1}
	Mu0	E-G94A/S153L	NA	NA	NA
	Mu10	Mu0-H145F/Y188A	2.0	4.2	2.1
	Mu14	Mu0-G94Q/H145F/Y188A	1.6	2.2	1.3
	P	PpYSDR	4.4×10^{-1}	2.3×10^{-1}	5.3×10^{-1}
	Mu17	P-M85S	4.5×10^{-1}	1.1	2.4

^aExperiments were performed in triplicate, and mean values are presented. ^bSub. = substrate. ^cNA = not available.

composed of a large open cavity C1 and a small closed cavity C2 that accommodate, respectively, the bulky and small groups at carbonyl carbon of the substrate, resulting in anti-Prelog selectivity. Based on the reaction mechanism of short-chain dehydrogenase,²¹ S143 stabilizes the substrate and Y156 functions as the catalytic base. The reaction is initiated by proton transfer from the hydroxyl of Y156 to the carbonyl oxygen of the substrate. Then, hydride in nicotinamide adenine dinucleotide (NADH) is transferred to the carbonyl carbon, which converts the carbonyl group of the substrate into a hydroxyl group.

Development of the prereaction state in computational simulations could be used to predict the enzyme's reactivity to the substrate.²⁸ In the case of dehydrogenases/reductases, the prereaction state forms when the hydroxyl oxygen (OH) of catalytic tyrosine forms a H-bond with the carbonyl oxygen of the substrate (O_{sub}) and meanwhile the hydrogen atom at C4N of NAD(P)H (H18_{NAD(P)H}) is close enough to the carbonyl carbon of the substrate (C_{sub}) for transfer of hydride. Therefore, the probability of prereaction-state formation was determined by calculating the proportion of conformation with distance between the O_{sub} and OH_{Y156} [designated as $d(O_{sub}-OH_{Y156}) \leq 2.8 \text{ \AA}$ and distance between C_{sub} and H18_{NADH} [designated as $d(C_{sub}-H18_{NADH}) \leq 3.0 \text{ \AA}$ according to the previous reports on hydride and proton transfer.^{29,30}

To evaluate the possibility of prereaction-state development, the model of Mu0 assembled with the difficult-to-reduce ketone **2a** in the orientation for producing R-alcohol (**2a_{ProR}**), designated as Mu0-**2a_{ProR}**, was constructed by docking, and two stages of MD simulation (T-state simulation and F-state

simulation) were performed successively. The structure of the lowest energy was chosen to represent the binding mode in each simulation. In the T-state simulation, complex Mu0-**2a_{ProR}** formed the prereaction state in the presence of distance restriction (Figure 2A). However, substrate **2a_{ProR}** was bound at the C1 cavity and far away from the active site when the restriction was released. The obvious difference in binding modes between the two simulations suggested the difficulty in formation of the prereaction state. The $d(O_{sub}-OH_{Y156})$ and $d(C_{sub}-H18_{NADH})$ in F-state simulation were 4.24 and 4.68 Å in average, respectively, and the proportion of "catalytic" conformations with both $d(O_{sub}-OH_{Y156}) \leq 2.8 \text{ \AA}$ and $d(C_{sub}-H18_{NADH}) \leq 3.0 \text{ \AA}$ was zero (Figure 3A), showing difficulty in completing the process of proton and hydride transfer. The failure of the Mu0-**2a_{ProR}** complex to develop into the prereaction state as predicted by computer simulation is consistent with the low conversion in the whole-cell reduction experiment.

It was found that the bulky residues H145 and Y188 are close to each other by hydrogen bonding (the proportion of $d(OH_{Y188}-NE2_{H145}) \leq 3.2 \text{ \AA}$ is as high as 78%), which forms a "beam" at the entry of cavity C2, holding **2a_{ProR}** back from the active site as revealed by the trajectory of Mu0-**2a_{ProR}** in F-state simulation. The energy contributions of residues comprising the substrate-binding pocket to the binding of **2a_{ProR}** in Mu0 were analyzed by preresidue energy decomposition of Mu0-**2a_{ProR}** in F-state simulation (Figure 3D). The result showed that the catalytic residues S143, Y156, and K160 made little energy contribution to **2a_{ProR}**'s binding to Mu0, suggesting the difficulty in realizing catalytic binding, proton transfer, and

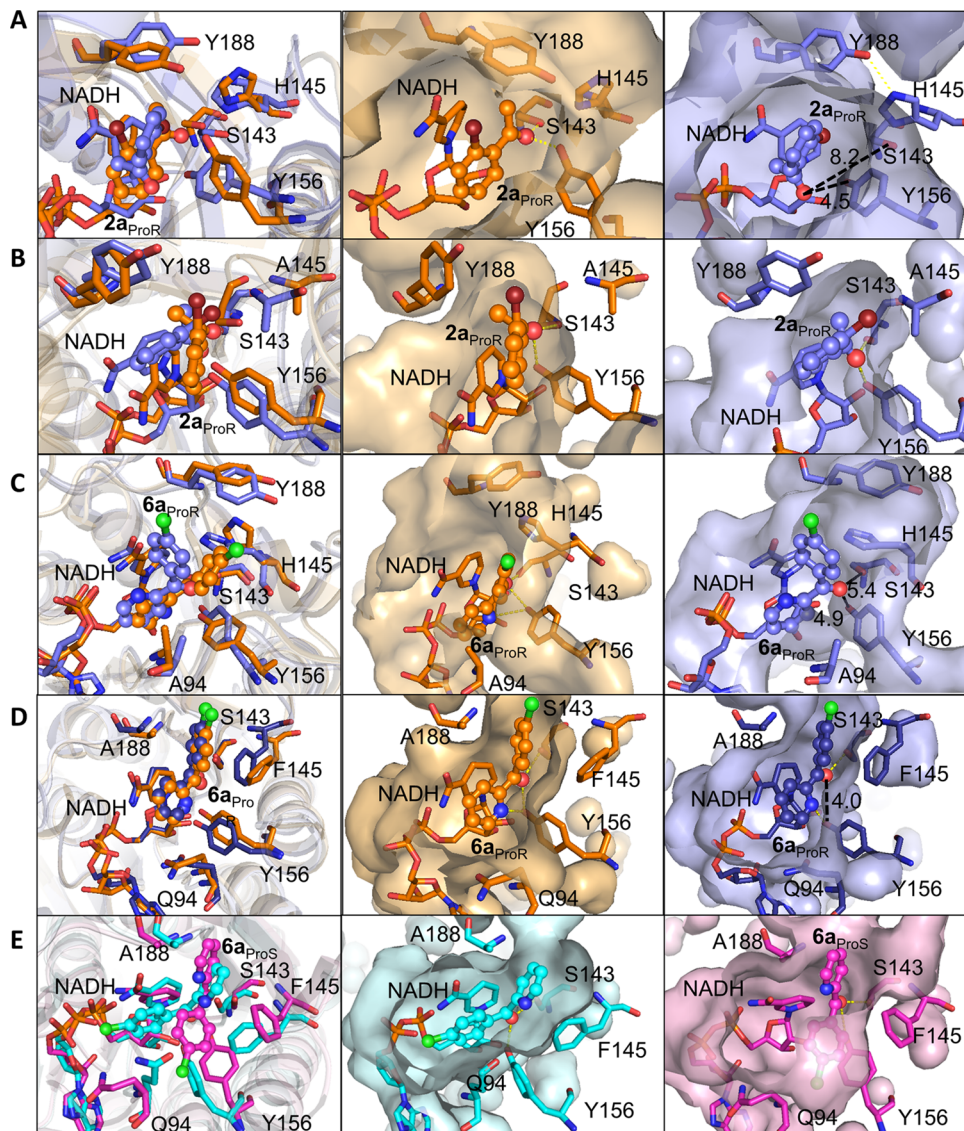


Figure 2. Binding modes of **2a** and **6a** to Mu0 and its variants in prereaction-state simulation and free-state simulation: (A) Binding modes of **2a_{ProR}** to Mu0 in prereaction-state simulation (orange) and free-state simulation (blue); (B) binding modes of **2a_{ProR}** to Mu1 in prereaction-state simulation (orange) and free-state simulation (blue); (C) binding modes of **6a_{ProR}** to Mu0 in prereaction-state simulation (orange) and free-state simulation (blue); (D) binding modes of **6a_{ProR}** to Mu14 in prereaction-state simulation (orange) and free-state simulation (blue); and (E) binding modes of **2a_{ProS}** to Mu14 in prereaction-state simulation (cyan) and free-state simulation (pink). Key residues are shown as sticks, and substrates are shown as balls and sticks. The hydrogen bonds are shown as yellow dashes, and the distances are shown with black dashes and values (Å).

electron transfer. The binding energy was mainly sourced from I93, A94, Y188, S199, and Y202. Noticeably, residues I93, A94, S199, and Y202 are located at cavity C1, and their high energy contributions in F-state simulation indicate high attraction of **2a_{ProR}** to cavity C1. Therefore, **2a_{ProR}** was trapped at the entrance of the substrate-binding pocket due to steric hindrance and strong attraction by cavity C1 and developed into noncatalytic conformation.

Similarly, high probability of hydrogen bonding between H145 and Y188 (proportion of $d(\text{OH}_{\text{Y}188}-\text{NE2}_{\text{H}145}) \leq 3.2 \text{ \AA}$ reaches 25%), obviously different binding modes between T-state and F-state simulations (Figure 2C), failure to form “catalytic” conformations (Figure 3B), and unsuitable energy distribution (Figure 3E) in the F-state simulation were found in complex Mu0 with **6a** in orientation for producing R-alcohol (**6a_{ProR}**), designated as Mu0-**6a_{ProR}**, suggesting the “beam” formed in the middle of the gourdlike substrate-binding pocket

as the major reason for the poor catalytic performance of Mu0 in reducing prochiral aryl ketones with bulky substituents at the carbonyl carbon. Therefore, H145 and Y188 were identified as the engineering targets.

EbSDR8 Mutants Designed with Flexible “Gourd” Neck Gained Activity toward the Bulky Substrates. To eliminate the steric hindrance at the entrance of the C2 cavity, H145 and Y188 were replaced with smaller residues (alanine, glycine, and cysteine, respectively), and the conversions of almost all of the substrates tested (except **6a**) were enhanced as expected to varying degrees (Table 1). However, the replacement resulted in enlargement of the cavity C2, and a large but unfit active center always leads to decline of enantioselectivity. For example, after replacing H145 with alanine (Mu1) and glycine (Mu3), the conversion of **4a** increased from 35 to >99%, but the ee value decreased from 67 to 51% or even reversed.

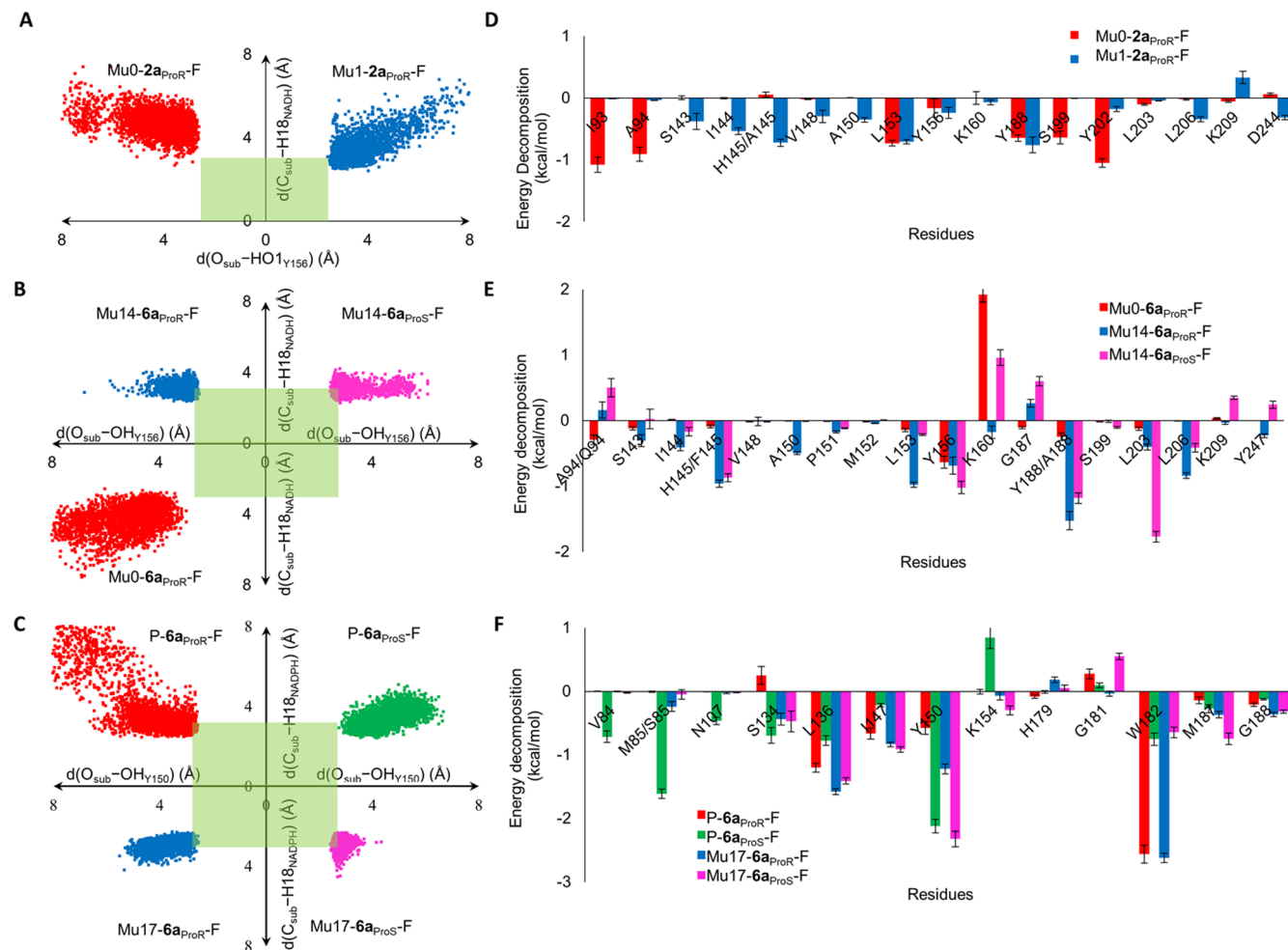


Figure 3. Conformation maps and energy decomposition of the residues in the substrate-binding pocket in free-state simulations. (A) Conformation maps of Mu0-2a_{ProR} (red) and Mu1-2a_{ProR} (blue); (B) conformation maps of Mu0-6a_{ProR} (red), Mu14-6a_{ProR} (blue), and Mu14-6a_{ProS} (pink); (C) conformation maps of P-6a_{ProR} (red), P-6a_{ProS} (green), Mu17-6a_{ProR} (blue), and Mu17-6a_{ProS} (pink); (D) energy contributions of residues in the substrate-binding pocket to binding of 2a_{ProR} in Mu0 (red) and Mu1 (blue); (E) energy contributions of residues in the substrate-binding pocket to binding of 6a_{ProR} in Mu0 (red) and Mu14 (blue) and 6a_{ProS} in Mu14 (pink); and (F) energy contributions of residues in the substrate-binding pocket to binding of 6a_{ProR} in P (red) and Mu17 (blue) and 6a_{ProS} in P (green) and Mu17 (pink). The limits of “catalytic distances”, namely, $d(O_{sub}-OH_{Y156}) \leq 2.8 \text{ \AA}$ (or $d(O_{sub}-OH_{Y150}) \leq 2.8 \text{ \AA}$) and $d(C_{sub}-H18_{NADH}) \leq 3.0 \text{ \AA}$ (or $d(C_{sub}-H18_{NADPH}) \leq 3.0 \text{ \AA}$), in panels A–C are colored by green.

Mutants with high conversion and ee value were selected for catalytic kinetic analysis. Compared with E and Mu0, almost all mutants had higher k_{cat} and k_{cat}/K_m in spite of increased K_m for the tested substrates (Table 2). The parallel increase of k_{cat} and K_m indicates a low degree of nonproductive binding.³¹ Although higher K_m means lower affinity to the substrate, a higher value of k_{cat} is more desirable because the high substrate load in application can fully cover the shortage of low affinity and high k_{cat} rather than k_{cat}/K_m represents high catalytic efficiency.³² Moreover, possible substrate inhibition can be relieved if the binding affinity is low.³³ Combining the results of whole-cell reduction and kinetic parameters, two mutants with excellent catalytic performance, Mu1 (Mu0-H145A) and Mu2 (Mu0-Y188A), were obtained. Mu1 efficiently reduced 1a and 2a into the corresponding R-alcohol with >99% conversion and >99% ee, whereas Mu2 efficiently reduced 3a and 5a into the corresponding R-alcohol with 95% conversion and >99% ee and 4a into S-alcohol with >99% conversion and >99% ee.

After the first round of mutagenesis, no satisfactory biocatalyst for reduction of 6a with two aromatic rings at the carbonyl carbon was obtained, indicating that single-point mutagenesis at position 145 or 188 cannot afford a cavity C2 large enough to accommodate the bulky 4-chlorophenyl substituent or 2-pyridyl substituent. In consideration of the delocalized pi bonds in both the 4-chlorophenyl ring and the 2-pyridyl ring, Y188 of Mu1, Mu2 and Mu3 or H145 of Mu4, Mu5, and Mu6 were replaced with the nonpolar phenylalanine to introduce a $\pi\cdots\pi$ interaction and meanwhile to further enlarge the cavity C2. Among these mutants, Mu10 (Mu0-H145F/Y188A) and Mu12 (Mu0-H145F/Y188G) reduced 6a with higher than 90% conversion (Table 3). However, they showed unsatisfactory enantioselectivity, with 91 and 84% ee for the R-product, respectively. To further improve the enantioselectivity of Mu10 toward 6a, a larger polar residue (Q94 or R94) was introduced to shrink the size of cavity C1 and meanwhile increase its polarity to attract the pyridine ring, taking into account the greater unevenness of the electron cloud the pyridine ring shows than the chlorobenzene ring.¹¹

Table 3. Mutagenesis for Reduction of Substrate 6a^a

sub. ^b	enzyme	description	conversion (%)	ee (%)
6a	Mu7	Mu0-H145A/Y188F	ND ^c	NA ^d
	Mu8	Mu0-H145C/Y188F	1.0	24 (R)
	Mu9	Mu0-H145G/Y188F	ND	NA
	Mu10	Mu0-H145F/Y188A	97	91 (R)
	Mu11	Mu0-H145F/Y188C	9.0	84 (R)
	Mu12	Mu0-H145F/Y188G	93	84 (R)
	Mu13	Mu0-G94R/H145F/Y188A	96	85 (R)
	Mu14	Mu0-G94Q/H145F/Y188A	99	98 (R)
P	PpYSDR		44	41 (S)
Mu15	P-M85A		91	95 (S)
Mu16	P-M85G		14	92 (S)
Mu17	P-M85S		>99	96 (S)

^aExperiments were performed in triplicate, and mean values are presented. ^bSub. = substrate. ^cND = not detected. ^dNA = not available.

The resulting mutant Mu14 (Mu0-G94Q/H145F/Y188A) reduced **6a** into the corresponding R-alcohol with 99% conversion and 98% ee.

As shown above, efficient variants for asymmetric reduction of bulky aryl ketones were created under the guidance of the T-/F-state comparative analysis. Compared with other rational design strategies using MD simulations, this approach could reveal the key residues causing poor reactivity in a more direct manner and help accurately identify the engineering targets.

Mutagenesis Improved the Affinity of Holoenzyme to the Target Substrates. The reaction catalyzed by dehydrogenase/reductases occurs in two steps. The apoenzyme first binds to the cofactor, forming holoenzyme, and then the holoenzyme binds to the substrates according to the kinetics of the interaction.³⁴ However, noncatalytic binding of the substrate to the apoenzyme can also occur. Only when the substrate binds to the holoenzyme can the reaction occur. Therefore, the difference in the affinity of the holoenzyme and apoenzyme to the substrate would decide the ratio of catalytic/noncatalytic conformation. The affinity of the apoenzyme to a certain substrate could be simply determined using the dissociation constant K_d and the Hill coefficient h , taking advantage of the measurable fluorescence quenching of the apoenzyme after substrate binding. However, variation in the free holoenzyme cannot be measured using this method due to loss of fluorescence after cofactor binding. Considering the strong fluorescence of NAD(P)H, the decrease of the free cofactor amount in the reaction was measured to quantify substrate binding of the holoenzyme. In this way, the dissociation constant K_d and the Hill coefficient h were determined for the apoenzyme and holoenzyme of the variants and their parent (Table 4).

For each substrate, the positive variant showed comparable $K_d^{\text{apoenzyme}}$ and $h^{\text{apoenzyme}}$ to those of its parent, indicating that the mutagenesis did not change the affinity of the apoenzyme to the substrates. In contrast, there was great difference in the affinity of the holoenzyme before and after mutagenesis. Compared with Mu0, Mu1 showed much lower $K_d^{\text{holoenzyme}}$ values for **1a** and **2a**, suggesting higher affinity of Mu1 to o-halogenated acetophenones than Mu0. The $h^{\text{holoenzyme}}$ values of Mu1 for **1a** and **2a** were greater than 1, while those of Mu0 were below 1, indicating that the mutagenesis altered the binding of the holoenzyme from negative cooperativity to positive cooperativity. Decreased $K_d^{\text{holoenzyme}}$ and increased

Table 4. Dissociation Constant K_d and Hill Coefficient h of Apoenzymes and Holoenzymes to the Substrates^a

sub. ^b	enzyme	$K_d^{\text{apoenzyme}}$	$h^{\text{apoenzyme}}$	$K_d^{\text{holoenzyme}}$	$h^{\text{holoenzyme}}$
1a	Mu0	4.4×10^2	1.0	1.3×10^3	6.0×10^{-1}
	Mu1	4.5×10^2	9.5×10^{-1}	6.4	1.9
2a	Mu0	2.6×10^2	1.3	9.0×10^3	6.6×10^{-1}
	Mu1	2.2×10^2	1.3	1.3	2.2
3a	Mu0	2.6×10^2	1.2	3.4×10^3	1.9
	Mu4	2.1×10^2	1.4	5.0×10^2	6.2×10^{-1}
4a	Mu0	2.4×10^3	8.3×10^{-1}	1.1×10^3	8.1×10^{-1}
	Mu4	1.9×10^3	6.8×10^{-1}	1.0×10^{-1}	3.2
5a	Mu0	2.4×10^2	9.3×10^{-1}	3.6×10^3	1.0
	Mu4	2.0×10^2	1.0	1.8×10	1.3
6a	Mu0	7.8	1.4	1.8×10^3	1.1
	Mu14	7.7	1.3	6.7×10	1.5
	P	1.6×10	1.1	6.4	1.3
Mu17		1.6×10	1.1	1.9	1.8

^aExperiments were repeated twice or thrice, and mean values are presented. ^bSub. = substrate.

$h^{\text{holoenzyme}}$ were observed for the positive variant in binding to **4a**, **5a**, and **6a**. For **3a**, the $K_d^{\text{holoenzyme}}$ value of Mu4 was far lower than that of Mu0, despite the lower $h^{\text{holoenzyme}}$ value than Mu0, suggesting the higher affinity of the Mu4 holoenzyme to substrate **3a** as the dominant factor for the promoted activity.

Comparative Analysis of Parent/Variant Structural Features Revealed the Mechanisms of Activity Enhancement toward Bulky Substrates. *Increased Consistency of Binding Modes in T-State and F-State Facilitates Easier Formation of the Prereaction State.* To illustrate the mechanisms behind the activity enhancement, the model of mutant Mu1 assembled with **2a_{ProR}** designated as Mu1-**2a_{ProR}** was built and compared with Mu0-**2a_{ProR}**. Unlike Mu0-**2a_{ProR}**, the binding mode of Mu1-**2a_{ProR}** in F-state simulation is coincident with that in T-state simulation (Figure 2B). The means of $d(O_{\text{sub}}-\text{OH}_{Y156})$ and $d(C_{\text{sub}}-\text{H}18_{\text{NADH}})$ of Mu1-**2a_{ProR}** were 3.7 and 3.5 Å, respectively, which were shorter than those of Mu0-**2a_{ProR}** (4.2 and 4.7 Å, respectively). The prereaction state could be more easily formed in Mu1-**2a_{ProR}** as judged from its higher proportion of $d(O_{\text{sub}}-\text{OH}_{Y156}) \leq 2.8$ Å and $d(C_{\text{sub}}-\text{H}18_{\text{NADH}}) \leq 3.2$ Å (5.6%), while the proportion in Mu0-**2a_{ProR}** was zero (Figure 3A). Higher probability of prereaction conformation is in favor of more productive conformation, consistent with the >35-fold higher k_{cat} of Mu1 than Mu0 (Table 2).

Enlargement of Cavity C2 Enables the Surrounding Residues To Contribute Energy to Prereaction-State Formation of Aryl Ketones with Bulky Side Chains. Preresidue energy decomposition of complexes Mu0-**2a_{ProR}** and Mu1-**2a_{ProR}** was compared to analyze the roles of every residue in substrate/enzyme binding (Figure 3D). In F-state simulation, residues located in cavity C2 (I144, H145, V148, A150, Y188, L206, and D244) and active site residues (S143, Y156, and K160) contributed more energy, while residues (I93, A94, S199, and Y202) located in the entrance of cavity C1 contributed less energy to **2a_{ProR}**'s binding in Mu1 than Mu0. In terms of the structure, more energy contribution of active site residues as well as balanced energy distribution in cavities C1 and C2 is beneficial to the formation of the prereaction state, and the distinct total energy decomposition profile of Mu0 and Mu1 was the major reason for the contrasting prereaction-state proportion and different binding

modes of **2a_{ProR}** in F-state simulation, which is supported by Mu1's ability to catalyze the reduction reaction.

A similar phenomenon was found in F-state simulation of Mu0-**6a_{ProR}** and Mu14-**6a_{ProR}**. The means of $d(O_{\text{sub}}-\text{OH}_{Y156})$ and $d(C_{\text{sub}}-\text{H18}_{\text{NADH}})$ in Mu0-**6a_{ProR}** were 5.1 and 4.3 Å, respectively, resulting in the null proportion of the prereaction state, while the means of $d(O_{\text{sub}}-\text{OH}_{Y156})$ and $d(C_{\text{sub}}-\text{H18}_{\text{NADH}})$ in Mu14-**6a_{ProR}** were both 3.0 Å, allowing the formation of the prereaction state with 21% probability (Figure 3B). Additionally, the mutagenesis succeeded in increasing the energy contribution of residues at the substrate-binding pocket to binding of the **6a_{ProR}** (Figure 3E). Replacing H145 and Y188 with phenylalanine and alanine, respectively, enlarged the cavity C2 of Mu14, making it large enough to accommodate the *p*-chlorobenzene ring (Figure 2D). Therefore, it was easier for Mu14-**6a_{ProR}** to develop into the prereaction state in F-state simulation, which was consistent with that in T-state simulation.

In short, the substitution of H145 or Y188 with alanine broke the hydrogen bond between sites 145 and 188 and meanwhile enlarged the cavity C2 for accommodating the aryl ketones with bulky side chains. Meanwhile, the balanced energy distribution of the substrate-binding pocket facilitated the formation of a stable productive conformation. As a result, the probability of prereaction conformation was obviously enhanced, as reflected by the higher activity determined.

Comparative Analysis of Prereaction States for R-Alcohol and S-Alcohol Production Revealed the Mechanisms of Improvement in Enantioselectivity.

Productive Conformation Is Formed at the Cost of Structural Fluctuation and Even Deformation of the Enzyme When the Substrate-Binding Orientation Is Unfavorable. In the prereaction complex, the orientation of substrate binding in Mu14 determines the product configuration. When **6a** locates its pyridine ring in cavity C1 and *p*-chlorophenyl ring in cavity C2, it will result in a *Si*-face attack of hydride from NADH and the delivery of *R*-alcohol. Otherwise, a *Re*-face attack occurs, and *S*-alcohol would be delivered. To investigate the mechanism for the high enantioselectivity Mu14 (Mu0-94Q145F188A) showed toward **6a**, the complexes with **6a** bound in the orientation for *R*-alcohol (designated as Mu14-**6a_{ProR}**) and *S*-alcohol (designated as Mu14-**6a_{ProS}**) production were comparatively analyzed by MD simulations. The binding models of Mu14-**6a_{ProR}** and Mu14-**6a_{ProS}** in F-state simulation were compared with those in T-state simulation (Figure 2D,E). Substitution of A94, H145, and Y188 with Q94, F145, and A188, respectively, generated a different substrate-binding pocket with a smaller cavity C1 and a larger cavity C2 in Mu14 as compared with Mu0. As a result, **6a** preferred to locate its smaller pyridine ring in cavity C1 and locate its larger *p*-chlorophenyl ring in cavity C2, which was favorable for *R*-product delivery. The conformations of **6a_{ProR}** and the residues in the substrate-binding pocket of Mu14 were consistent in T-state and F-state simulations. In contrast, **6a_{ProS}** and its surrounding residues showed significant deviation in those two simulations of Mu14-**6a_{ProS}**. Root-mean-square deviation (RMSD) is generally used to describe the fluctuation of the enzyme/substrate complex.³⁵ To get comparable results for different complexes, the structure of the lowest energy was chosen as a reference for RMSD calculation to represent the fluctuation degree of the complex. The higher RMSD of Mu14-**6a_{ProS}** as compared with Mu14-**6a_{ProR}** in F-state simulation revealed that the binding of **6a_{ProS}** led to higher

fluctuation of Mu14-**6a_{ProS}** (Figure S3A). Considering the greater deviation of binding modes between two simulations and the higher RMSD in F-state simulation of Mu14-**6a_{ProS}**, it is reasonable to conclude that only at the cost of great structural fluctuation and tendency of deformation did the Mu14 form the prereaction state with **6a_{ProS}**, which might account for the **6a_{ProR}** preference of Mu14.

Difference in Probability of Prereaction-State Formation for R- and S-Alcohols Predicted by Computational Simulation Is Consistent with the High Enantioselectivity. The $d(O_{\text{sub}}-\text{OH}_{Y156})$ and $d(C_{\text{sub}}-\text{H18}_{\text{NADH}})$ of complexes Mu14-**6a_{ProR}** and Mu14-**6a_{ProS}** in F-state simulation were analyzed. The $d(C_{\text{sub}}-\text{H18}_{\text{NADH}})$ and $d(O_{\text{sub}}-\text{OH}_{Y156})$ were almost the same in the two complexes (3.0 and 3.0 Å in Mu14-**6a_{ProR}** and 3.0 and 3.1 Å in Mu14-**6a_{ProS}**). However, the proportion of "catalytic" conformation with both $d(O_{\text{sub}}-\text{OH}_{Y156}) \leq 2.8$ Å and $d(C_{\text{sub}}-\text{H18}_{\text{NADH}}) \leq 3.0$ Å in Mu14-**6a_{ProR}** was higher than that in Mu14-**6a_{ProS}** (21 vs 15%) (Figure 3B), suggesting that formation of the prereaction state was easier for **6a_{ProR}** than **6a_{ProS}**, and it is consistent with the high enantioselectivity Mu14 showed toward **6a**, with 98% ee for the *R*-product.

Difference in Energy Contributions of Residues at the Substrate-Binding Pocket to Substrate Binding in the Two Orientations Results in High Enantioselectivity. Preresidue energy decomposition of Mu14-**6a_{ProR}** and Mu14-**6a_{ProS}** was performed for analysis of energy contributions of residues at the substrate-binding pocket (Figure 3E). In F-state simulation, there are fewer residues offering positive values of energy decompositions in Mu14-**6a_{ProR}** than Mu14-**6a_{ProS}**, suggesting higher possibility of Mu14 to accept **6a_{ProR}** than **6a_{ProS}**. Although the active site residue Y156 offered higher energy contribution in Mu14-**6a_{ProS}**, S143 made no contribution to the binding of **6a_{ProS}**. Moreover, K160 showed a positive value of energy decomposition with 0.96(12) kcal/mol of energy decomposition to Mu14-**6a_{ProS}**, which is unfavorable for accomplishing the function of catalytic residues and cofactor. On the contrary, the active sites S143, Y156, and K160 all made contribution to Mu14-**6a_{ProR}** with -0.30(9), -0.67(13), and -0.18(9) kcal/mol of energy decomposition, respectively, which is favorable for realizing proton transfer and electron transfer. The mutated sites F145 and A188 also made great contribution to the binding of **6a** to Mu14, as revealed by the negative value of energy decomposition. However, A188 contributed more energy to Mu14-**6a_{ProR}** than Mu14-**6a_{ProS}**. Considering the higher energy contribution of their surrounding residues (S143, I144, A150, P151, M152, K160, L206, K209, and Y247) in Mu14-**6a_{ProR}** than Mu14-**6a_{ProS}** and Mu0-**6a_{ProR}**, the replacement of polar H145 and Y188 by smaller hydrophobic F145 and A188, respectively, increased the energy contribution of their surrounding residues, consistent with the high activity and partly explained the excellent enantioselectivity of Mu14 toward **6a**. Noticeably, compared with Mu0-**6a_{ProR}**, Q94 had a repulsion effect on the binding of **6a** in each orientation as revealed by the positive value of energy decomposition. However, the repulsion effect was weaker in Mu14-**6a_{ProR}** than Mu14-**6a_{ProS}**, as suggested by the lower energy decomposition for the former, and its surrounding residue L153 made significantly more energy contribution to Mu14-**6a_{ProR}** than Mu14-**6a_{ProS}** and Mu0-**6a_{ProR}**, consistent with the easier prereaction-state formation in Mu14-**6a_{ProR}** than Mu14-**6a_{ProS}**.

Based on the above results, the substitution of H145 and Y188 with F145 and A188, respectively, enabled the enzyme to reduce **6a**, and the replacement of A94 with Q94 facilitated the asymmetric reduction of Mu14 for producing *R*-alcohol, which together led to efficient production of (*R*)-(4-chlorophenyl)-(pyridin-2-yl) methanol [(*R*)-CPMA].

Adaption of the Design Principle to PpYSDR Further Validated Its Effectiveness. Although (*S*)-CPMA is a more valuable intermediate for synthesizing the antiallergy drug bepotastine,¹¹ its synthesis is difficult to realize using EbSDR8 or its variants considering the hydrophobic environment in its cavity C2 (Figure S2A,B). To obtain a biocatalyst for synthesis of (*S*)-CPMA and meanwhile to further validate the effectiveness of the rational design strategy, another short-chain dehydrogenase/reductase PpYSDR from *Pseudomonas putida* ATCC 12633 (GenBank: AP013070.1) that shows moderate *S*-selectivity toward **6a** (with 44% conversion and 41% ee) was redesigned.

The predicted model of the PpYSDR holoenzyme was built and optimized as that of Mu0. The assessment considered the predicted structure of PpYSDR reasonable with a VERIFY value of 88% and an ERRAT value of 89, and >99% of the residues were located in the allowed region as shown by the Ramachandran plot. The cavity C2 of PpYSDR has an open structure due to the short substrate-binding loop (fragments 179–196) (Figure S1D), making it large enough for accommodating the pyridine ring or the *p*-chlorophenyl ring of **6a**. Little deviation was observed between the binding modes in T-state simulation and F-state simulation in P-**6a**_{ProR} and P-**6a**_{ProS} (Figure S4A,B). On the one hand, the difference in the polarity of the two cavities (Figure S2C) led to localization of the pyridine ring and *p*-chlorophenyl ring of **6a** in cavities C2 and C1, respectively (in the orientation for producing *S*-alcohol), which is also reflected by the higher energy contributions of the binding pocket made to P-**6a**_{ProS} than to P-**6a**_{ProR} in F-state simulation (Figure 3F). On the other hand, the relatively smaller cavity C1 and larger cavity C2 allowed PpYSDR to bind **6a**_{ProR} with less structural fluctuation (Figure S3B). The contradiction between **6a**_{ProS}-preferential polarity distribution and **6a**_{ProR}-preferential binding pocket size is consistent with PpYSDR's insufficient enantioselectivity toward **6a**. However, the shorter mean distances of *d*(O_{sub}—OH_{Y150}) and *d*(C_{sub}—H18_{NADPH}) observed in P-**6a**_{ProS} than P-**6a**_{ProR} (Figure 3C) and the *S*-conformation preference determined in catalysis suggest that the **6a**_{ProS}-preferential polarity distribution is predominant. To further improve the *S*-selectivity of PpYSDR toward **6a**, the enzyme was redesigned by enlarging the cavity C1 for better accommodation of the *p*-chlorophenyl ring. The position of M85, corresponding to A94 in Mu0, was predicted to be a key site in modulating the size of cavity C1 and was chosen as the engineering target.

To enlarge the cavity C1, M85 was replaced by smaller residues such as alanine, glycine, and serine, generating Mu15 (PpYSDR-85A) and Mu17 (PpYSDR-85S) with enhanced activity and improved *S*-selectivity toward **6a** (Table 3). In particular, Mu17 reduced **6a** into *S*-CPMA with >99% conversion and 96% ee. The catalytic kinetics of PpYSDR and Mu17 showed that Mu17 had about 5-fold higher *k*_{cat} and almost the same *K*_m toward **6a** as compared with PpYSDR (Table 2).

In F-state simulation, Mu17 was able to bind **6a** in both orientations as in T-state simulation, which is the same as

PpYSDR (Figure S4). However, the RMSD of Mu17-**6a**_{ProS} was lower than that of Mu17-**6a**_{ProR} (Figure S3B), indicating that the enlargement of cavity C1 successfully decreased the structural fluctuation of Mu17-**6a**_{ProS} and promoted binding of Mu17 to **6a**_{ProS} rather than **6a**_{ProR}. The proportion of Mu17-**6a**_{ProS} forming the prereaction state was 27%, while that of Mu17-**6a**_{ProR} was only 4.4% (Figure 3C). The great difference in possibility of prereaction-state formation toward two orientations indicates that Mu17 prefers **6a**_{ProS} over **6a**_{ProR}. In terms of energy decomposition, the mutagenesis at position 85 had a great influence on the surrounding residues. Compared with the energy decompositions in P-**6a**_{ProR} and P-**6a**_{ProS} (Figure 3F), I147 and M187 in Mu17 contributed more, while V84, S85, and N107 contributed less energy to the binding of **6a** in both orientations. In addition, the preference of cavity C1 to accommodate the *p*-chlorophenyl ring over the pyridine ring was decided by I147 and M187, as judged from their higher energy contributions to **6a**_{ProS} than **6a**_{ProR}. Although the residues at cavity C2 did not show obvious preference to the *p*-chlorophenyl ring or the pyridine ring, the catalytic residues Y150 and K154 contributed more energy to **6a**_{ProS} than **6a**_{ProR}, in accordance with the easier occurrence of catalysis in Mu17-**6a**_{ProS} than Mu17-**6a**_{ProR}. Therefore, the replacement of M85 with serine provided Mu17 with **6a**_{ProS}-preferential polarity distribution and binding pocket size, resulting in an excellent biocatalyst for reducing **6a** into *S*-CPMA.

CONCLUSIONS

This study investigated the reason for the low activity or insufficient enantioselectivity of short-chain dehydrogenase/reductase toward prochiral aryl ketones with bulky side chains via enzyme/substrate complex docking and comparative analysis of the binding modes in T-state and F-state simulations. Accordingly, residues that decide the relative size of the two cavities in the substrate-binding pocket were identified as the engineering targets. Rational design of short-chain dehydrogenase/reductase was performed to reconstruct a suitable substrate-binding pocket, using EbSDR8-G94A/S153L and PpYSDR as parent enzymes. Finally, variants with both excellent activity and enantioselectivity for efficient asymmetric reduction of 2'-chloroacetophenone, 2'-bromoacetophenone, propiophenone, ethyl 2-oxo-4-phenylbutyrate, 3-chloropropiophenone, and (4-chlorophenyl) 2-pyridyl ketone were obtained. MD simulations indicated that a suitable substrate-binding pocket is beneficial for accommodating and binding the target substrates in the prereaction state with less structural fluctuation, and proper energy distribution facilitates the formation of the prereaction state. The results in this study verify the efficiency of the protein redesign based on comparative analysis of enzyme-/substrate-binding modes between T-state simulation and F-state simulation in creating dehydrogenases/reductases with both excellent activity and enantioselectivity toward unnatural substrates and suggest the suitable relative sizes of two cavities in the substrate-binding pocket together with balanced energy distribution as the mechanisms for activity enhancement or enantioselectivity improvement of short-chain dehydrogenases/reductases.

MATERIALS AND METHODS

Microorganisms and Chemicals. Recombinant *Escherichia coli* BL21 (DE3) strains harboring pET30a-EbSDR8-

G94A/S153L and pET30a-PpYSDR have been constructed in a previous study.^{7,8} Acetophenone (**0a**) was purchased from Guanhua Co., Ltd. (Nanjing, China). 2'-Chloroacetophenone (**1a**) was purchased from Kaisai Chemical Co. Ltd. (Shanghai, China). 2'-Bromoacetophenone (**2a**) was purchased from Ditong Chemical Co. Ltd. (Changzhou, China). Propiophenone (**3a**) was purchased from Jinweida Chemical Co. Ltd. (Changzhou, China). 2-Oxo-4-phenylbutyrate (**4a**) was purchased from Puyuan Chemical Co. Ltd. (Taicang, China). 3-Chloropropiophenone (**5a**) was obtained from Alfa Chemical Co., Ltd. (Zhengzhou, China). (4-Chlorophenyl) 2-pyridyl ketone (**6a**) was obtained from Xiangzhe Technology Co., Ltd. (Hangzhou, China). Their corresponding S- and R-alcohols were supplied by XHSynbio Co., Ltd. (Hangzhou, China). Nicotinamide adenine dinucleotide (NADH), nicotinamide adenine dinucleotide phosphate (NADPH), and isopropyl- β -D-thiogalactoside (IPTG) were purchased from Aladdin Bio-Chem Technology Co., Ltd. (Shanghai, China). TransStart FastPfu Fly DNA polymerase and DMT enzyme (an improved DpnI) were purchased from TransGen Biotech Co. Ltd. (Beijing, China). All other chemicals and reagents were purchased from authentic suppliers, were at least of reagent grade, and used without further purification.

Mutagenesis. Site-directed mutagenesis was carried out by polymerase chain reaction (PCR) using mutagenic primers (listed in Table S1) and plasmid pET30a-EbSDR8-G94A/S153L or pET30a- PpYSDR as the template according to the manufacturer's instructions of TransStart FastPfu Fly DNA polymerase. The PCR product (2 μ L) digested by the DMT enzyme was transformed into 100 μ L of *E. coli* BL21 (DE3)-competent cells, and the transformants verified by DNA sequencing were incubated for protein expression.

Protein Expression. *E. coli* BL21 (DE3) cells carrying the recombinant plasmid were cultivated in 1 mL of LB medium containing Kanamycin (50 μ g/mL) at 37 °C and 220 rpm for 10 h. The culture was inoculated into 50 mL of Kanamycin-containing LB medium and grown at 37 °C and 220 rpm. When the culture's optical density ($OD_{600\text{nm}}$) reached 0.6–0.7, 0.1 mM IPTG was added to induce the enzyme expression at 25 °C and 220 rpm for an additional 12 h. The cells were harvested by centrifugation (4000 rpm, 5 min) at 4 °C, washed with 0.9% NaCl solution, and resuspended in sodium phosphate buffer (100 mM, pH 7.5), adjusting the cell concentration to 100 mg/mL.

Whole-Cell Reduction. The bioreduction was carried out at 37 °C and 220 rpm for Mu0 and its variants and at 30 °C and 220 rpm for PpYSDR and its variants. For every substrate, the reaction mixture (500 μ L) consisted of 50 mM substrate, 25 mg of wet enzyme-containing cells (250 μ L of the above-mentioned resuspended cells), and 25 μ L of isopropanol as the cosubstrate. After 2 h of reaction, the organic phase was extracted with ethyl acetate. The conversion and ee value were determined by high-performance liquid chromatography (HPLC) or gas chromatography (GC) equipped with chiral columns as summarized in Table S2. For **0a**, **1a**, **2a**, and **3a**, the extraction was dried over anhydrous Na_2SO_4 before GC detection. For **4a**, **5a**, and **6a**, the extraction was evaporated under vacuum, dissolved in isopropanol, and dried over anhydrous Na_2SO_4 before HPLC detection.

Protein Purification. The cells overexpressing the target enzyme were lysed by ultrasonication in an ice bath, and the supernatant was collected by centrifugation (12 000 rpm, 10 min) at 4 °C. The protein was purified using affinity

chromatography with a HisTrap FF crude column (GE) using AKTAprime plus (GE). The sample was loaded onto a Ni-NTA affinity column and subsequently washed with washing buffer (50 mM imidazole, 20 mM sodium phosphate, 500 mM NaCl, pH 7.5) at a flow rate of 5 mL/min. The target protein fractions were eluted with elution buffer (500 mM imidazole, 20 mM sodium phosphate, 500 mM NaCl, pH 7.5) at the same flow rate. The imidazole was wiped off from purified protein by storage buffer (20 mM sodium phosphate, 10% (v/v) glycerol, pH 7.5) with a PD-10 desalting column (GE). Protein concentration was measured by the Bradford assay.

Determination of Kinetic Parameters. Enzyme activities of EbSDR8 and its mutants were determined by measuring the decrease in the absorbance of NADH at 340 nm ($\epsilon = 6.0/\text{mM}/\text{cm}$) using a spectrophotometer 1510 (Thermo Fisher Scientific) at 37 °C, while the activities of PpYSDR and its variants were determined by measuring the decrease in the absorbance of NADPH at 340 nm ($\epsilon = 5.3/\text{mM}/\text{cm}$) at 30 °C. The assay mixture (200 μ L) was composed of 150 μ L of potassium phosphate buffer (50 mM, pH 7.5), 20 μ L of substrates (0.2–20 mM), 10 μ L of NAD(P)H (5 mM), and 20 μ L of purified protein with an appropriate concentration. One unit of enzyme activity is defined as the amount of enzyme catalyzing the oxidation of 1 μ mol NAD(P)H per minute. All experiments were conducted in triplicate. The activities at different substrate concentrations were used to calculate the kinetic parameters by nonlinear regression according to the Michaelis–Menten equation.

Determination of Affinity by Fluorescence Experiments. The affinity of enzymes to substrates was analyzed with a FluoroMax-4 fluorescence spectrophotometer (Horiba, Paris, French). The binding of substrates to apoenzymes was measured by monitoring the quenching of intrinsic enzyme fluorescence upon incremental addition of the substrate. The samples consisted of 4 μ M enzyme and 20–2000 μ M substrate in potassium phosphate buffer (50 mM, pH 7.5). Emission spectra (300–500 nm) were recorded at 280 nm excitation.

The binding of substrate to holoenzymes was measured by monitoring the decreased fluorescence of NAD(P)H. The samples contained 4 μ M enzyme, 20–2000 μ M substrate, and 66 μ M cofactor in potassium phosphate buffer (50 mM, pH 7.5). The 455 nm emission was recorded at 348 nm excitation after the reaction reaching equilibrium as judged by kinetic fluorimetry.

The K_d value was determined by the nonlinear least-squares method. The model is expressed by a simple Hill equation with consideration of the Hill coefficient h and the dissociation constant K_d : $\ln \frac{1-\theta}{\theta} = \ln(K_d) - h \times \ln(S)$, where θ is the fractional saturation of the enzyme (i.e., number of occupied sites/total number of sites) and S is substrate concentration.³⁶

Molecular Docking. The homology models of Mu0 and its mutants were built based on the crystal structure of an NADH-dependent 1-(4-hydroxyphenyl)-ethanol dehydrogenase Hped from *Aromatoleum aromaticum* EbN1 (Protein Data Bank Code 4URF),²² which shares 52% amino acid sequence identity with Mu0. For PpYSDR and its mutants, the homology models were built with a carbonyl reductase PA4079 from *Pseudomonas aeruginosa* PAO1 (Protein Data Bank Code SWQO),³⁷ which shares 39% amino acid sequence identity with PpYSDR. The predicted models were further optimized with Amber18,²⁷ and the quality of the final models

was assessed by Verify 3D,³⁸ ERRAT,³⁹ and the Ramachandran plot.⁴⁰ Molecular dockings were performed using AutoDock 4.⁴¹ The conformations with hydrogen-bond interactions between carbonyl oxygen of the substrate and hydroxyl of the active site Tyr (Y156 in Mu0 and its mutants, and Y150 in PpYSDR and its mutants) or a less than 4.5 Å distance between carbonyl carbon and C4 atoms of NAD(P)H were selected preferentially to generate the starting conformations of enzyme–substrate complexes (Figure S5).

Molecular Dynamics Simulations. The force fields for the substrates and cofactors were constructed using the antechamber module in Amber18 and were used to generate the topology and coordinate files for the system with the LEaP module in Amber18 in company with the Amber force fields FF14SB, GAFF2, and TIP3P. The missing atoms and hydrogen were added automatically as the complexes were loaded. The systems were solvated in an explicit TIP3P water box and extended 8.0 Å along each dimension. Sodium ions were added to neutralize each system. Then, the topology and coordinate files for systems were generated.

Each system was subjected to a three-stage energy minimization (minimize solvate, then minimize protein, finally minimize the whole system) before MD simulation. Each minimization stage included 2500 steps of steepest descent minimization and 2500 steps of conjugate gradient minimization. For T-state simulation, the $d(O_{\text{sub}}-\text{OH}_{\text{Y156}})$ [$d(O_{\text{sub}}-\text{OH}_{\text{Y150}})$ for the PpYSDR system] and $d(C_{\text{sub}}-\text{H18}_{\text{NADH}})$ [$d(C_{\text{sub}}-\text{H18}_{\text{NADPH}})$ for the PpYSDR system] were restrained to 2.8 and 3.0 Å, respectively, using a harmonic vibrational potential with a force constant of 500 kcal/(mol·Å²). In the presence of distance restriction, the system was heated from 0 to 300 K at constant volume in 50 ps with the protein restricted, equilibrated at constant pressure in 50 ps with the protein restricted, and equilibrated for 500 ps without restriction of the protein. After equilibration, normal temperature and pressure (NPT) simulation was conducted for 8 ns to produce trajectories of T-state simulation, and then constraints of distances were released and another 8 ns of NTP simulation was run for the trajectory production of F-state simulation.

For T-state simulation or F-state simulation, the frame of the lowest total energy was chosen to represent the structure of the enzyme–substrate complex. The RMSD referring to the lowest total energy structure was calculated, and more than 3000 frames of continuous trajectories that showed consistent RMSD were collected for analysis of “catalytic” distances [$d(O_{\text{sub}}-\text{OH}_{\text{Y156}})$ and $d(C_{\text{sub}}-\text{H18}_{\text{NADH}})$ for the Mu0 system and $d(O_{\text{sub}}-\text{OH}_{\text{Y150}})$ and $d(C_{\text{sub}}-\text{H18}_{\text{NADPH}})$ for the PpYSDR system] and energy decomposition of residues in the substrate-binding pocket (residues around the substrate within 6 Å) to the binding of substrate with the MM-PBSA method in Amber18.

ASSOCIATED CONTENT

Supporting Information

The Supporting Information is available free of charge at <https://pubs.acs.org/doi/10.1021/acscatal.9b04778>.

Tables for primer list, HPLC and GC analytic conditions, figures for substrate-binding pockets of different dehydrogenase/reductases, contact potential analysis of substrate-binding pockets, RMSD analysis, binding modes of 6a to P and Mu17 in prereaction-state

simulation and free-state simulation, starting conformation of enzyme–substrate complexes (PDF)

AUTHOR INFORMATION

Corresponding Authors

*E-mail: ljuan@fzu.edu.cn (J.L.).
*E-mail: yelidan@zju.edu.cn (L.-D.Y.).
*E-mail: yuhongwei@zju.edu.cn (H.-W.Y.).

ORCID

Bing-Mei Su: 0000-0001-7785-3798
Juan Lin: 0000-0003-4202-285X
Li-Dan Ye: 0000-0002-6248-8457
Hong-Wei Yu: 0000-0002-9144-4496

Author Contributions

The manuscript was written through contributions of all authors. All authors have given approval to the final version of the manuscript. B.M.S., L.D.Y., H.W.Y., and J.L. designed the experiments and prepared the manuscript. A.P.L. constructed the two parents of this study EbSDR8-G94A/S153L and PpYSDR. B.M.S. performed mutagenesis, protein expression, whole-cell reduction, purification, and determination of catalytic kinetics. B.M.S., Z.H.S., and M.N. conducted the molecular dynamics simulations. All authors analyzed and discussed the results.

Notes

The authors declare no competing financial interest.

ACKNOWLEDGMENTS

This work was financially supported by the National Key Research and Development Program of China (Grant no. 2018YFA0901800), the Natural Science Foundation of China (Grant nos. 21576234 and 21776244), and Zhejiang Provincial Natural Science Foundation of China (Grant no. LY18B060001).

ABBREVIATIONS

F-state simulation, free-state simulation; GC, gas chromatography; HPLC, high-performance liquid chromatography; IPTG, isopropyl-β-D-thiogalactoside; MD, molecular dynamics; NADH, nicotinamide adenine dinucleotide; NADPH, nicotinamide adenine dinucleotide phosphate; NTP, normal temperature and pressure; PCR, polymerase chain reaction; (R)-CPMA, (R)-(4-chlorophenyl)-(pyridin-2-yl) methanol; RMSD, root-mean-square deviation; (S)-CPMA, (S)-(4-chlorophenyl)-(pyridin-2-yl) methanol; SDR, short-chain dehydrogenase/reductase; T-state simulation, prereaction-state simulation

REFERENCES

- (1) Huang, S.; Li, W.; Chen, L.; Xu, J.; Hong, R. Chemoenzymatic Construction of Chiral Alkenyl Acetylenic Alcohol, a Key Building Block to Access Diastereoisomers of Polyacetylenes. *Bioprocess. Bioproc.* **2015**, *2*, 2–10.
- (2) Liang, J.; Lalonde, J.; Borup, B.; et al. Development of a Biocatalytic Process as an Alternative to the (−)-DIP-Cl-Mediated Asymmetric Reduction of a Key Intermediate of Montelukast. *Org. Process Res. Dev.* **2010**, *14*, 193–198.
- (3) Otoguro, K.; Ishiyama, A.; Namatame, M.; et al. Selective and Potent in Vitro Antitrypanosomal Activities of Ten Microbial Metabolites. *J. Antibiot.* **2008**, *61*, 372–378.
- (4) Homola, P.; Kurák, T. s.; Illeová, V.; Polakovi, M. Cultivation of *Pichia capsulata* as a Whole-Cell Biocatalyst with NADH-Dependent

- Alcohol Dehydrogenase Activity for R -1-phenylethanol Production. *Food Bioprod. Process.* **2015**, *96*, 126–132.
- (5) Li, Y. Y.; Yu, S.; Shen, W.; Gao, J. Iron-, Cobalt-, and Nickel-Catalyzed Asymmetric Transfer Hydrogenation and Asymmetric Hydrogenation of Ketones. *Acc. Chem. Res.* **2015**, *48*, 2587–2598.
- (6) Choudhury, S.; Baeg, J.-O.; Park, N.-J.; Yadav, R. K. A Solar Light-Driven, Eco-Friendly Protocol for Highly Enantioselective Synthesis of Chiral Alcohols via Photocatalytic/Biocatalytic Cascades. *Green Chem.* **2014**, *16*, 4389–4400.
- (7) Li, A.; Ye, L.; Yang, X.; Yang, C.; Gu, J.; Yu, H. Structure-Guided Stereoselectivity Inversion of a Short-Chain Dehydrogenase/Reductase towards Halogenated Acetophenones. *Chem. Commun.* **2016**, *52*, 6284–6287.
- (8) Li, A.; Ye, L.; Yang, X.; Wang, B.; Yang, C.; Gu, J.; Yu, H. Reconstruction of the Catalytic Pocket and Enzyme-Substrate Interactions to Enhance the Catalytic Efficiency of a Short-Chain Dehydrogenase/Reductase. *ChemCatChem* **2016**, *8*, 3229–3233.
- (9) Zhang, R.; Xu, Y.; Xiao, R. Redesigning alcohol dehydrogenases/reductases for more efficient biosynthesis of enantiopure isomers. *Biotechnol. Adv.* **2015**, *33*, 1671–1684.
- (10) Zheng, G.-W.; Liu, Y.-Y.; Chen, Q.; Huang, L.; Yu, H.-L.; Lou, W.-Y.; Li, C.-X.; Bai, Y.-P.; Li, A.-T.; Xu, J.-H. Preparation of Structurally Diverse Chiral Alcohols by Engineering Ketoreductase CgKRI. *ACS Catal.* **2017**, *7*, 7174–7181.
- (11) Zhou, J.; Wang, Y.; Xu, G.; Wu, L.; Han, R.; Schwaneberg, U.; Rao, Y.; Zhao, Y. L.; Zhou, J.; Ni, Y. Structural Insight into Enantioselective Inversion of an Alcohol Dehydrogenase Reveals a “Polar Gate” in Stereorecognition of Diaryl Ketones. *J. Am. Chem. Soc.* **2018**, *140*, 12645–12654.
- (12) Wu, X.; Yang, S.; Yu, H.; Ye, L.; Su, B.; Shao, Z. Improved Enantioselectivity of *E. coli* BioH in Kinetic Resolution of Methyl (S)-3-cyclohexene-1-carboxylate by Combinatorial Modulation of Steric and Aromatic Interactions. *Biosci., Biotechnol., Biochem.* **2019**, *83*, 1263–1269.
- (13) Chen, C.; Huang, Y.; Jiang, X.; Xiao, Y. Binding Free-Energy Calculation of an Ion-Peptide Complex by Constrained Dynamics. *Phys. Rev. E* **2013**, *87*, No. 062705.
- (14) Jensen, M. Ø.; Park, S.; Tajkhorshid, E.; Schulten, K. Energetics of Glycerol Conduction through Aquaglyceroporin GlpF. *Proc. Natl. Acad. Sci. USA* **2002**, *99*, 6731–6736.
- (15) Crespo, A.; Martí, M. A.; Estrin, D. o. A.; Roitberg, A. E. Multiple-Steering QM-MM Calculation of the Free Energy Profile in Chorismate Mutase. *J. Am. Chem. Soc.* **2005**, *127*, 6940–6941.
- (16) Li, A.; Ye, L.; Wu, H.; Yang, X.; Yu, H. Characterization of an Excellent Anti-Prelog Short-Chain Dehydrogenase/Reductase EbSDR8 from *Empedobacter brevis* ZJUY-1401. *J. Mol. Catal. B: Enzym.* **2015**, *122*, 179–187.
- (17) Li, A.; Ye, L.; Guo, F.; Yang, X.; Yu, H. Biocatalytic Anti-Prelog Reduction of Prochiral Ketones with Whole Cells of a Newly Isolated Strain *Empedobacter brevis* ZJUY-1401. *J. Mol. Catal. B: Enzym.* **2015**, *117*, 31–37.
- (18) Yang, G.; Ou, Z.; Yao, S.; Xu, J. Asymmetric Reduction of 3-chloropropiophenone to (S)-3-chloro-1-Phenylpropanol Using Immobilized *Saccharomyces cerevisiae* CGMCC 2266 cells. *J. Mol. Catal. B: Enzym.* **2009**, *57*, 83–88.
- (19) Chen, M.; Zhang, X. Y.; Xing, C. G.; Zhang, C.; Zheng, Y. C.; Pan, J.; Xu, J. H.; Bai, Y. P. Efficient Stereoselective Synthesis of Structurally Diverse γ - and δ -Lactones Using an Engineered Carbonyl Reductase. *ChemCatChem* **2019**, *11*, 2600–2606.
- (20) Prelog, V. Specification of the Stereospecificity of Some Oxidoreductase by Diamond Lattice Sections. *Pure Appl. Chem.* **1964**, *9*, 119–130.
- (21) Höffken, H. W.; Duong, M.; Friedrich, T.; Breue, M.; Hauer, B.; Reinhardt, R.; Rabus, R.; Heider, J. Crystal Structure and Enzyme Kinetics of the (S)-Specific 1-Phenylethanol Dehydrogenase of the Denitrifying Bacterium Strain EbN1. *Biochemistry* **2006**, *45*, 82–93.
- (22) Büsing, L.; Hoffken, H. W.; Breuer, M.; Wohlbrand, L.; Hauer, B.; Rabus, R. Molecular Genetic and Crystal Structural Analysis of 1-(4-Hydroxyphenyl)-Ethanol Dehydrogenase from ‘*Aromatoleum aromaticum*’ EbN1. *J. Mol. Microbiol. Biotechnol.* **2015**, *25*, 327–339.
- (23) Kazlauskas, R. J.; Weissflock, A. N. E.; Rappaport, A. T.; Cuccia, L. A. A Rule to Predict Which Enantiomer of a Secondary Alcohol Reacts Faster in Reactions Catalyzed by Cholesterol Esterase, Lipase from *Pseudomonas cepacia*, and Lipase from *Candida rugosa*. *J. Org. Chem.* **1991**, *56*, 2656–2665.
- (24) Ahmed, S.; Kazlauskas, R.; Morinville, A.; Grochulski, P.; et al. Enantioselectivity of *Candida rugosa* Lipase Toward Carboxylic Acids: A Predictive Rule from Substrate Mapping and X-Ray Crystallography. *Biocatalysis* **1994**, *9*, 209–225.
- (25) Min, B.; Park, J.; Sim, Y. K.; Jung, S.; Kim, S. H.; Song, J. K.; Kim, B. T.; Park, S. Y.; Yun, J.; Park, S.; Lee, H. Hydrogen-Bonding-Driven Enantioselective Resolution against the Kazlauskas Rule to Afford Gamma-Amino Alcohols by *Candida rugosa* Lipase. *Chem-biochem* **2015**, *16*, 77–82.
- (26) Waterhouse, A.; Bertoni, M.; Bienert, S.; Studer, G.; Tauriello, G.; Gumienny, R.; Heer, F. T.; de Beer, T. A. P.; Rempfer, C.; Bordoli, L.; Lepore, R.; Schwede, T. SWISS-MODEL: Homology Modelling of Protein Structures and Complexes. *Nucleic Acids Res.* **2018**, *46*, 296–303.
- (27) Salomon-Ferrer, R.; Case, D. A.; Walker, R. C. An Overview of the Amber Biomolecular Simulation Package. *Wiley Interdiscip. Rev.: Comput. Mol. Sci.* **2013**, *3*, 198–210.
- (28) Shi, T.; Liu, L.; Tao, W.; Luo, S.; Fan, S.; Wang, X.-L.; Bai, L.; Zhao, Y.-L. Theoretical Studies on the Catalytic Mechanism and Substrate Diversity for Macrocyclization of Pikromycin Thioesterase. *ACS Catal.* **2018**, *8*, 4323–4332.
- (29) Torres, R. A.; Schiott, B.; Bruice, T. C. Molecular Dynamics Simulations of Ground and Transition States for the Hydride Transfer from Formate to NAD⁺ in the Active Site of Formate Dehydrogenase. *J. Am. Chem. Soc.* **1999**, *121*, 8164–8173.
- (30) Salna, B.; Benabbas, A.; Champion, P. M. Proton-Coupled Electron Transfer and the “Linear Approximation” for Coupling to the Donor-Acceptor Distance Fluctuations. *J. Phys. Chem. A* **2017**, *121*, 2199–2207.
- (31) Kuusk, S.; Valjamae, P. When Substrate Inhibits and Inhibitor Activates: Implications of Beta-Glucosidases. *Biotechnol. Biofuels* **2017**, *10*, 7.
- (32) Eisenthal, R.; Danson, M. J.; Hough, D. W. Catalytic Efficiency and kcat/KM: a Useful Comparator? *Trends Biotechnol.* **2007**, *25*, 247–249.
- (33) Hamnevik, E.; Maurer, D.; Enugala, T. R.; Chu, T.; Löfgren, R.; Dobritzsch, D.; Widersten, M. Directed Evolution of Alcohol Dehydrogenase for Improved Stereoselective Redox Transformations of 1-Phenylethane-1,2-diol and Its Corresponding Acyloin. *Biochemistry* **2018**, *57*, 1059–1062.
- (34) Mu, X. Q.; Xu, Y.; Yang, M.; Sun, Z. H. Steady-State Kinetics of the Oxidation of (S)-1-phenyl-1,2-ethanediol Catalyzed by Alcohol Dehydrogenase from *Candida parapsilosis* CCTCC M203011. *J. Mol. Catal. B: Enzym.* **2006**, *43*, 23–28.
- (35) Xie, Y.; An, J.; Yang, G.; Wu, G.; Zhang, Y.; Cui, L.; Feng, Y. Enhanced Enzyme Kinetic Stability by Increasing Rigidity within the Active Site. *J. Biol. Chem.* **2014**, *289*, 7994–8006.
- (36) Zhang, R.; Xu, Y.; Sun, Y.; Zhang, W.; Xiao, R. Ser67Asp and His68Asp Substitutions in *Candida parapsilosis* Carbonyl Reductase Alter the Coenzyme Specificity and Enantioselectivity of Ketone Reduction. *Appl. Environ. Microbiol.* **2009**, *75*, 2176–2183.
- (37) Li, S.; Teng, X.; Su, L.; Mao, G.; Xu, Y.; Li, T.; Liu, R.; Zhang, Q.; Wang, Y.; Bartlam, M. Structure and Characterization of a NAD(P)H-Dependent Carbonyl Reductase from *Pseudomonas aeruginosa* PAO1. *FEBS Lett.* **2017**, *591*, 1785–1797.
- (38) Eisenberg, D.; Lüthy, R.; U.Bowie, J. VERIFY3D: Assessment of Protein Models with Three-Dimensional Profiles. *Methods Enzymol.* **1997**, *277*, 396–404.
- (39) Colovos, C.; Yeates, T. O. Verification of Protein Structures: Patterns of Nonbonded Atomic Interactions. *Protein Sci.* **1993**, *2*, 1511–1519.

(40) Lovell, S. C.; Davis, I. W.; III, W. B. A.; Bakker, P. I. W. d.; Word, J. M.; Prisant, M. G.; Richardson, J. S.; Richardson, D. C. Structure Validation by C α Geometry: Phi, Psi and C β Deviation. *Proteins* **2003**, *50*, 437–450.

(41) Morris, G. M.; Huey, R.; Lindstrom, W.; Sanner, M. F.; Belew, R. K.; Goodsell, D. S.; Olson, A. J. AutoDock4 and AutoDockTools4: Automated Docking with Selective Receptor Flexibility. *J. Comput. Chem.* **2009**, *30*, 2785–2791.